Nano Research

Open Access

Research Article

Revealing the electrochemistry of all-solid-state Li-CO_2 batteries via *in-situ* and cryogenic-transmission electron microscopy

Zhiying Gao[1,§], Hui Xu[5,6,§], Qiushi Dai[1], Yali Liang[1], Runhui Zhao[1], Bo Wang[3], Zhaoyu Rong[1], Jinyan Li[1], Ailin Bao[1], Jiace Cheng[3], Wen Li[7], Hailong Qiu[1], Feng Huo[4,5,6], Jingzhao Chen[4] ✉, Yongfu Tang[1,3] ✉, and Jianyu Huang[1,2] ✉

[1] *Clean Nano Energy Center, State Key Laboratory of Metastable Materials Science and Technology, Yanshan University, Qinhuangdao 066004, China*
[2] *School of Materials Science and Engineering, Xiangtan University, Xiangtan 411105, China*
[3] *Hebei Key Laboratory of Applied Chemistry, College of Environmental and Chemical Engineering, Yanshan University, Qinhuangdao 066004, China*
[4] *Longzihu New Energy Laboratory, Henan Key Laboratory of Energy Storage Materials and Processes, Zhengzhou Institute of Emerging Industrial Technology, Zhengzhou 450003, China*
[5] *Center of Ionic Liquids and Green Energy, Beijing Key Laboratory of Solid State Battery and Energy Storage Process; Institute of Process Engineering, Chinese Academy of Sciences, Beijing 100190, China*
[6] *University of Chinese Academy of Sciences, Beijing 100049, China*
[7] *Shandong Zhaowen New Energy Technology Co., Ltd., Weifang 262100, China*
§ *Zhiying Gao and Hui Xu contributed equally to this work.*

Cite this article: *Nano Research*, **2026**, *19*, 94908658. https://doi.org/10.26599/NR.2026.94908658

ABSTRACT: Li-CO_2 batteries have attracted wide attentions due to their dual roles both in CO_2 capture and as sustainable energy storage devices. However, the electrochemistry of Li-CO_2 batteries, especially for all-solid-state (ASS) Li-CO_2 batteries, remains unclear due to the complicated electro-catalytic reactions. Here, we first reveal the reaction and failure mechanisms of ASS Li-CO_2 batteries using Ag nanowires (NWs) as the cathode catalyst. During discharge, the Ag NWs react with Li ions to *in-situ* form Li-Ag alloy, which facilitates the CO_2 reduction to generate $LiAg_3O_2$ nanoparticles dispersed uniformly in film-like Li_2CO_3 and amorphous carbon (a-C). During charge, Li_2CO_3 is decomposed to CO_2 under the catalysis of Ag. During both charge and discharge, the Ag NW surfaces are corroded and disintegrated into nanocrystalline Ag, $LiAg_3O_2$, and single-atom Ag, and the continuously accumulated a-C layer wraps up the broken Ag NWs, isolating the Ag NWs with CO_2 gas, thus shutting off the electrochemical reactions in the Li-CO_2 batteries. This study unveils the electrochemistry and failure mechanisms of ASS Li-CO_2 batteries, which provides a scientific basis for developing CO_2-based carbon fixation and renewable energy storage strategies.

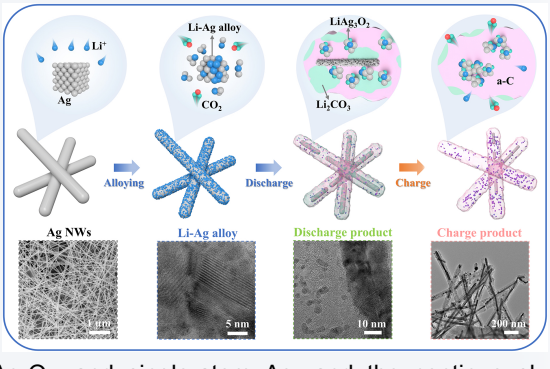

KEYWORDS: Li-CO_2 batteries, all-solid-state, electrochemistry, Li-Ag alloy, *in-situ* and cryogenic-transmission electron microscopy (*in-situ* and cryo-TEM)

1 Introduction

The increasing CO_2 emissions from fossil fuel consumption have caused global warming, leading to serious climate change [1–5]. To address this issue, the capture and utilization of CO_2 from the atmosphere are urgently needed to combat the greenhouse effect. In this context, the lithium-carbon dioxide (Li-CO_2) battery has drawn particular attentions due to its dual-effects of both CO_2 fixation and as a potential electrochemical energy storage device [6, 7]. However, their practical application is hindered by the sluggish kinetics of the electrochemical CO_2 reduction reaction (CRR) and CO_2 evolution reaction (CER) [8]. Significant efforts have been made toward developing highly efficient catalysts to facilitate the sluggish CRR

Received: January 23, 2026; **Revised:** March 9, 2026
Accepted: March 21, 2026

✉Address correspondence to Jingzhao Chen, chenjingzhao@lnelab.ac.cn; Yongfu Tang, tangyongfu@ysu.edu.cn; Jianyu Huang, jhuang@ysu.edu.cn

and CER in Li-CO_2 batteries [9–11]. RuO_2, Cu/NC, and high-entropy alloys were reported as highly efficient to reversible decomposition of discharge products [12–15]. Among the various Li-CO_2 batteries, those based on conventional liquid organic electrolyte with porous separators face challenges such as the side reactions between electrolyte and cathode catalysts, the vaporization of liquid electrolyte, and the shuttle of CO_2 from cathode to anode [16–18]. In contrast, all-solid-state (ASS) Li-CO_2 batteries using ASS electrolyte may mitigate the detrimental electrolyte/electrode reactions and the growth of lithium dendrites [19–24]. However, fundamental mechanistic studies of ASS Li-CO_2 batteries are scarce. Consequently, the reaction process and electrocatalysis mechanisms of both the electrochemical CRR and CER, as well as the failure mechanism of the ASS Li-CO_2 batteries, remain unclear [25–31]. As such, comprehensive understanding of the reaction and failure mechanisms is of paramount importance for the development of both CO_2 fixation and Li-CO_2 battery systems.

Previous Li-CO_2 batteries mostly use carbon-based cathode and liquid electrolyte, rendering the mechanistic understanding difficult as the CRR and CER products contain carbon, the source of which is complicated by the use of carbon-based cathode and the liquid organic electrolyte, as both may participate the CRR and CER reactions [32]. To this end, it is necessary to construct Li-CO_2 batteries without carbon cathode and liquid electrolyte so that the effect of the carbon cathode and the liquid electrolyte can be excluded. Therefore, using carbon-free cathode and organic free electrolyte to assemble ASS Li-CO_2 batteries provides a clean system for exploring the underlying electrochemical reaction and failure mechanisms. Among the present inorganic solid electrolytes, garnet-type $Li_{6.4}La_3Zr_{1.4}Ta_{0.6}O_{12}$ (LLZTO) is considered the most promising candidate due to its high ionic conductivity and excellent mechanical properties, although the studies on the LLZTO based ASS Li-CO_2 battery are scarce [33, 34]. Furthermore, microstructure and phase characterization of the charge/discharge products are challenging due to the air and electron beam sensitivity of the reaction products [35–37]. The advent of cryogenic transmission electron microscopy (Cryo-TEM) brings new opportunity to characterize the beam sensitive discharge/charge products and investigate the complex reaction and failure mechanisms in ASS Li-CO_2 batteries, because Cryo-TEM freezes the samples to near liquid nitrogen temperature, thus minimizes the electron beam damage to the sample and avoids the effect of the H_2O and CO_2 contaminations in trace air during the sample transfer on the true structure of the discharge/charge productions, while preserving the pristine states of the samples under characterizations.

Herein, we first comprehensively studied the reaction and failure mechanisms of ASS Li-CO_2 battery with carbon-free and binder-free Ag nanowires (NWs) as the cathode catalysts, and LLZTO as the solid electrolyte. Combining advanced analytical techniques, including cryo-TEM and density functional theory (DFT) calculation, we reveal that the Li-Ag alloy *in-situ* forms to facilitate the CO_2 reduction kinetics via generating $LiAg_3O_2$ nanoparticles which are uniformly dispersed in film-like Li_2CO_3 and amorphous carbon (a-C). The formed Li_2CO_3 can be decomposed by the catalysts of Ag during charging, while a-C remains. Moreover, a direct visualization of the a-C accumulation on the Ag NWs and irreversible consumption of Ag NWs is clearly demonstrated by *in-situ* aberration-corrected environmental transmission electron microscopy (ETEM).

2 Results and discussion

Figure 1(a) shows a schematic of carbon-free and binder-free three-dimensional (3D) Ag NW framework cathode catalysts with high porosity in the ASS Li-CO_2 batteries. The Ag NWs are uniformly dispersed on the LLZTO pellets, forming a cross-linking network. To improve the interfacial contacts between the Ag NW network and the LLZTO pellets, an intermediate layer composed of nanometer Au with a thickness of ~ 80 nm was deposited between the Ag NWs and LLZTO surface using an ion sputtering technology (Figs. S1(a) and S1(b) in the Electronic Supplementary Material (ESM)). As shown in Fig. S2 in the ESM, the X-ray diffraction measurements (XRD) pattern of as-synthesized LLZTO matches well with the standard pattern of cubic garnet structure (PDF No. 45-0109). The cross-section scanning electron microscopy (SEM) images of the anode and the cathode catalysts interface of the battery show the intimate contact of Li anode/LLZTO interface (Fig. 1(b)) and LLZTO/Au/Ag NW interface (Fig. 1(c)). For the Ag NWs, a high fraction of pore volume is observed in the SEM image, which is essential to provide space for accommodating the solid discharge products of the ASS Li-CO_2 battery (Fig. 1(d)). The Li^+/e^- mixed conducting 3D framework is ensured by the interconnected Ag NWs, which facilitates CO_2 permeability. Previously, the Li^+ diffusion coefficient of Ag metal was measured to be 10^{-6} $cm^2 \cdot s^{-1}$ [38–40].

Figure 1(e) shows TEM image of a pristine Ag NW, which displays a face-centered cubic (FCC) structure (JCPDS No. 04-0783), as confirmed by the corresponding sharp electron diffraction pattern (EDP) taken along the [110] zone axis (Fig. 1(f)). The Ag NWs are grown along the $[1\bar{1}0]$ direction with a twin crystal structure (Fig. 1(g)). High-resolution TEM (HRTEM) image (Fig. 1(h)) reveals the high crystallinity of the Ag NW, and the lattice planes in the HRTEM are indexed as $(1\bar{1}1)$, (002), and $(\bar{1}11)$ planes of Ag, respectively. The high-angle annular dark-field-scanning transmission electron microscopy (HAADF-STEM) image and the corresponding fast Fourier transform (FFT) pattern of the Ag NW match the atomic structure model (insets in Fig. 1(i)) of FCC Ag along the [110] zone axis. A low magnification of HAADF image (Fig. 1(j)) shows the morphology of the pristine Ag NWs, and the corresponding energy dispersive X-ray spectroscopy (EDS) elemental mapping (Figs. 1(k) and 1(l)) indicates that the Ag NWs are clean without impurities.

As shown in Fig. 2(a), at a current density of 1 $\mu A \cdot cm^{-2}$ and 80 °C, the ASS Li-CO_2 battery with an ~ 80 nm-thick Au intermediate layer supported Ag NWs (Li|LLZTO|Au/Ag NWs) exhibits an areal capacity of 0.102 $mAh \cdot cm^{-2}$. In addition, the Au layer thickness of Li|LLZTO|Au/Ag NWs battery was increased to ~ 160 nm (Fig. S3 in the ESM), and the performance improvement was not obvious. Therefore, we adopted ~ 80 nm as the Au interlayer thickness in all subsequent experiments. For comparison, the ASS Li-CO_2 battery using the pure Ag NW cathode catalysts without the Au intermediate layer (Li|LLZTO|Ag NWs) contributes a discharge capacity of 0.062 $mAh \cdot cm^{-2}$, which is smaller than that of the Li|LLZTO|Au/Ag NWs cell. Both capacity values are much higher than that derived from the sole Au layer coated battery (Li|LLZTO|Au) of 0.2 $\mu Ah \cdot cm^{-2}$. As shown in Fig. S4 in the ESM, there are two semicircles in the electrochemical impedance spectroscopy (EIS). The semicircle in the high-frequency region represents the bulk phase resistance of Li^+ in the electrolyte, and the semicircle in the low-frequency region denotes the electrolyte/cathode interface resistance. Apparently, the interfacial

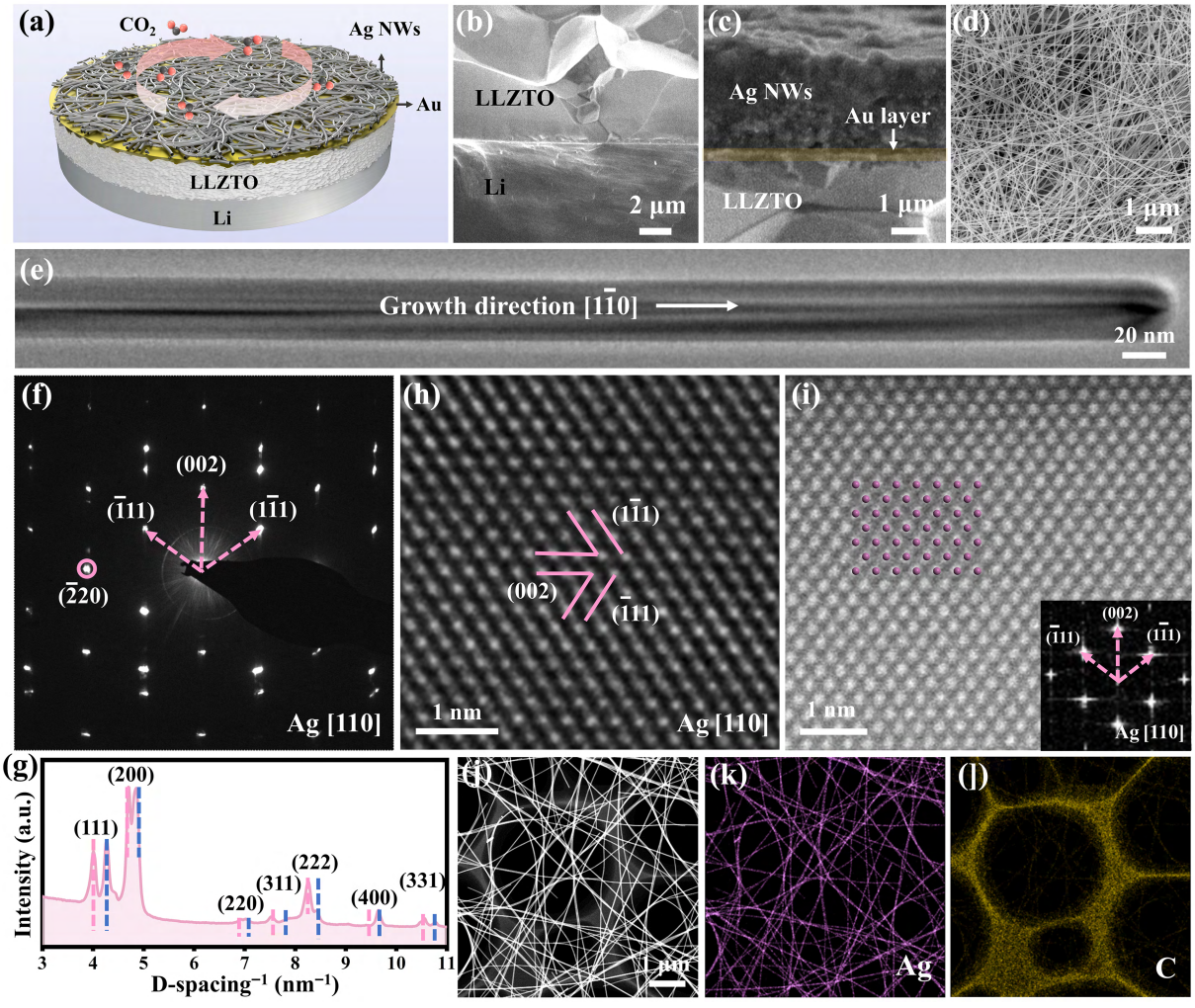

Figure 1 TEM characterizations of the pristine Ag cathode in a Li|LLZTO|Au/Ag cell in CO_2 gas. (a) Schematic illustration of solid-state Li-CO_2 batteries with a dense LLZTO ceramic pellet and a 3D Ag NW framework. ((b) and (c)) Cross-section SEM images of the anode and cathode interface of the battery. (d) The SEM image of the pristine Ag NWs. (e) A low magnification TEM image of a pristine Ag nanowire and (f) the EDP of the initial structural of the Ag NWs. (g) The diffraction integral of (f). (h) HRTEM image of the pristine Ag NW. (i) Atomic resolution HAADF image and the corresponding FFT of Ag NW viewed along the [110] direction, which agrees well with the structural models overlaid on the images. ((j)–(l)) The STEM-EDS elemental mapping of the Ag NWs. Purple and yellow represent Ag and C elements, respectively.

resistance of Li|LLZTO|Au/Ag NWs battery is lower than that of Li|LLZTO|Ag NWs battery, which is ascribed to the intimate contact between the Au layer and the LLZTO pellet. As shown in SEM images, the Ag NW surface with the Au as the intermediate layer is completely covered with discharge products (Figs. S5(a) and S5(b) in the ESM). Figures S5(c)–S5(e) in the ESM show that the discharge product formation sites on the Ag NW surface without the Au intermediate layer are not uniformly distributed. These results suggest that the synergistic effect between the Ag NW catalysts and Au coating on the LLZTO in the cathode plays an important role in the discharge reaction.

The electrochemical properties of the ASS Li-CO_2 batteries were further evaluated using galvanostatic discharge/charge curves and cyclic voltammetry (CV) tests. Figures 2(b) and 2(c), and Fig. S6(a) in the ESM show the discharge curves at different cycles of the as-assembled ASS Li-CO_2 batteries with the Ag NWs dispersed on the Au layer with the specific capacity being limited to 500, 200, and 50 mAh·g^{-1}. Compared with the charge/discharge curve of Li|LLZTO|Au/multiwall carbon nanotubes (MWCNTs) battery (Fig. S6(b) in the ESM), the Li|LLZTO|Au/AgNWs batteries have lower overpotential in the charge/discharge curves and stable discharge/charge voltage plateaus, indicating that the latter possesses excellent catalytic activity and stable cycling performance [41]. The CV curves (Fig. 2(d)) show a pair of CRR and CER peaks at ~ 2.2 and 3.5 V, and the interval between the CRR-CER peaks shows an increasing trend with the increase in the number of cycles. The EIS results of the ASS Li-CO_2 batteries before and after cycles indicate a significant increase in interfacial resistance (Fig. 2(e)), which implies the deterioration of the interface between the electrolyte and the cathode after cycles. Raman spectroscopy of the discharged cathode exhibits three peaks at ~ 1088, 1420, and 1600 cm^{-1}, which are assigned to Li_2CO_3, the D band, and G band of carbon, respectively (Fig. 2(f)). Raman spectroscopy of the charged cathode exhibits two halo peaks centered at 1420 and 1600 cm^{-1}, which are from a-C. XRD analysis (Fig. 2(g)) of the discharged cathode exhibits peaks corresponding to $LiAg_3O_2$, Li_2CO_3, and a-C, and the charge products are $LiAg_3O_2$, a-C, and a small amount of Li_2CO_3.

The morphology, phase structure, and composition of the discharge product were characterized by Cryo-TEM. The SEM

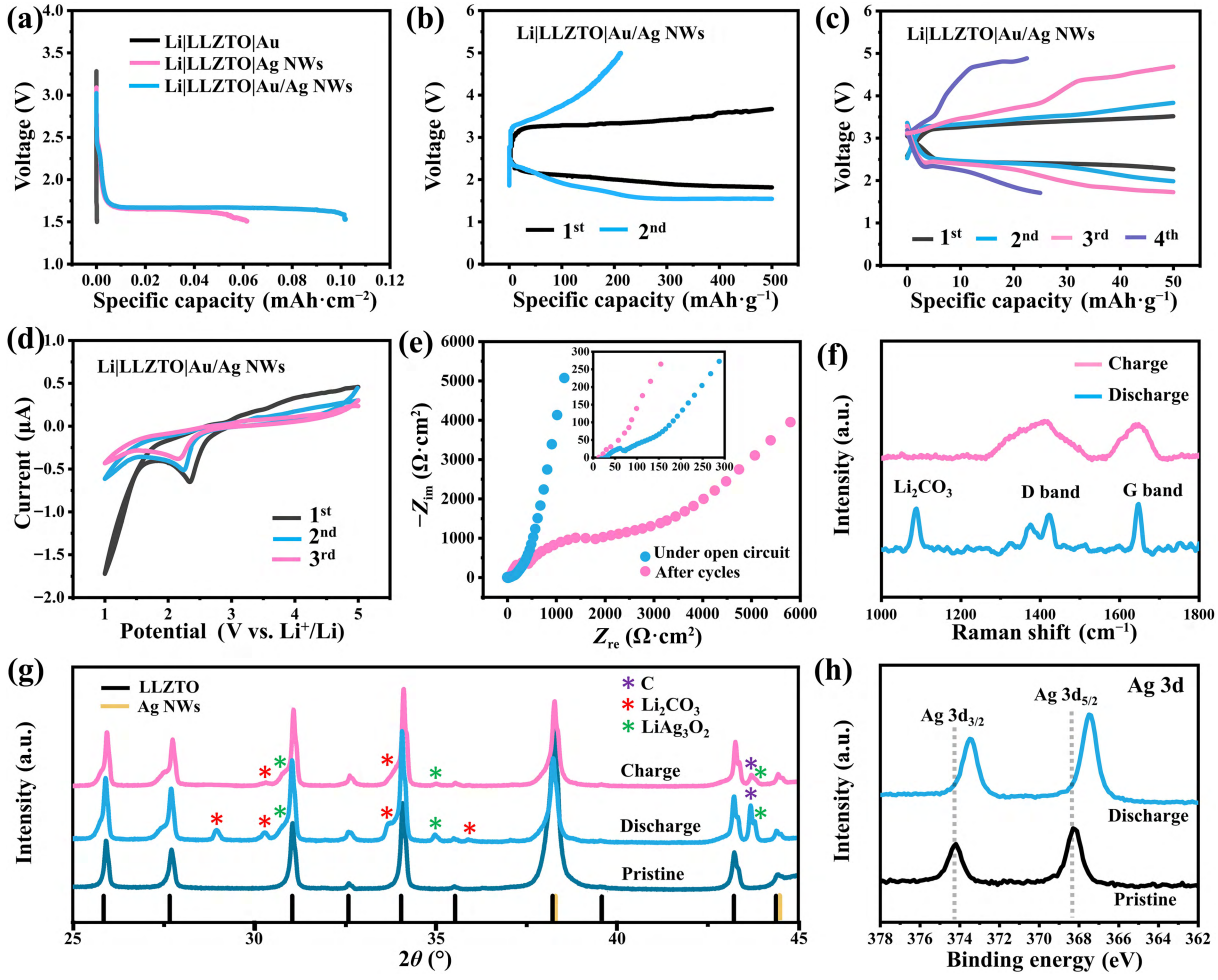

Figure 2 Electrochemical performance and characterization of the Li-CO_2 cells. (a) First discharge curves of the Li|LLZTO|Au, Li|LLZTO|Ag NWs, and Li|LLZTO|Au/Ag NWs cells at 80 °C and 1 μA·cm^{-2}. ((b) and (c)) Cycling performances of the Li|LLZTO|Au/Ag NWs cell at 80 °C and 25 mA·g^{-1} with the voltage being limited to 1.5–5.0 V and the capacities being limited to (b) 500 and (c) 50 mAh·g^{-1}. (d) The CV curves of the battery. (e) The Nyquist plots of the Li|LLZTO|Au/Ag NWs before and after cycles at 80 °C. (f) Raman spectroscopy of the discharged and charged cathodes. (g) XRD patterns of the pristine, discharged, and charged cathodes. (h) XPS of Ag 3d spectra of the cathode before and after discharge.

images (Fig. 3(a), and Figs. S7(a) and S7(b) in the ESM) show large number of beads on the Ag NWs, exhibiting pearl-necklace-like morphology. The sizes of the beads range from 500 to 1000 nm (Figs. S7(c)–S7(f) in the ESM). Cryo-TEM images (Fig. 3(b)) show that the discharged Ag NWs are covered with a thin film-like product. The selected-area electron diffraction (SAED) rings (Figs. 3(c) and 3(d)) of regions I and II in Fig. 3(b), as well as the corresponding diffraction integrals (Fig. S8 in the ESM) of the discharge products, can be indexed as Li-Ag alloy, $LiAg_3O_2$, and Li_2CO_3. HAADF-STEM image (Fig. 3(e)) and the corresponding elemental mapping (Figs. 3(f)–3(h)) indicate the homogeneous distribution of C and O within the film-like discharge product layer. The electron energy loss spectroscopy (EELS) spectra (Figs. S9(a)–S9(c) in the ESM) confirm that the film-like discharge product is Li_2CO_3. The Cryo-TEM image (Fig. 3(i)) and the local magnified image (Fig. 3(j)) reveal that numerous nanoparticles (NPs) with a size of about 5 nm emerge in the coating layer near the Ag NW surface, and these NPs are uniformly dispersed in the film. Cryo-HRTEM image (Fig. 3(k)) and local magnified images (Figs. 3(l) and 3(m)) with the FFT patterns (Figs. 3(n) and 3(o)) indicate that the discharge products are nanocrystalline Li_2CO_3 and a-C. Cryo-HRTEM image (Fig. 3(p)) and the inverse FFT (IFFT) of the corresponding local enlarged image (Fig. 3(q)) indicate the growth of crystalline Li_2CO_3 at the surface of the Ag NW, and the two phases maintain a semi-coherent interface. Isolated nanocrystalline Li_2CO_3 with a size of ~ 5 nm along the [$\bar{1}$23] zone axis dispersed in an amorphous matrix is also detected (Fig. 3(r)). In conclusion, the film-like discharge product layer is composed of nanocrystals Li_2CO_3 distributed in a-C matrix.

The Cryo-TEM image (Fig. S10(a) in the ESM) and the corresponding magnified images (Figs. S10(b)–S10(d) in the ESM) clearly demonstrate that the crystal lattice structure changes from an ordered arrangement of the Ag phase with [110] zone axis to the formation of local amorphous regions. The local magnified images with the corresponding IFFT and FFT patterns (Figs. S11(a)–S11(d) in the ESM) are indexed to the Li-Ag intermetallic compound with a composition of $Li_{33.44}Ag_{18.56}$ along the [35$\bar{1}$], [241], and [123] zone axes, respectively [42]. The X-ray photoelectron spectroscopy (XPS) analysis (Fig. 2(h)) shows two peaks at 367.4 and 373.6 eV corresponding to $3d_{5/2}$ and $3d_{3/2}$ of the Ag species, respectively. The negative shift of the binding energy values compared to that of the pristine Ag NWs (368.2 and 374.5 eV, respectively) indicates the formation of Li-Ag alloy during the discharge process [43]. HAADF-STEM image (Fig. 3(s), and Figs. S12(a) and S12(e) in the

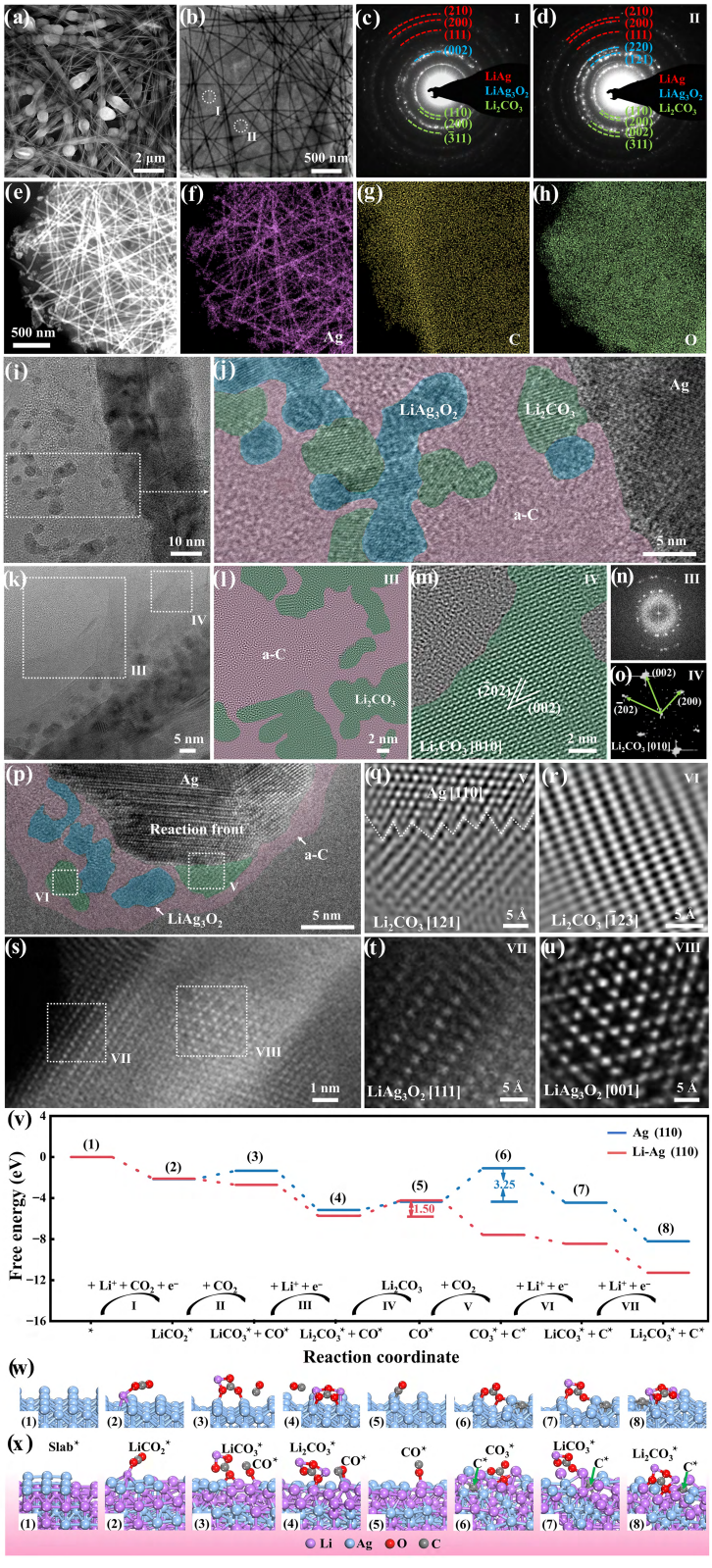

Figure 3 Electron microscopy characterizations of the discharge products and DFT calculations of the CRR thermodynamics. (a) SEM image of the discharge cathode. (b) Cryo-TEM image of the cathode after discharge. ((c) and (d)) EDPs acquired from ircular regions I and II in (b). ((e)–(h)) HAADF-STEM image of the cathode after discharge and the corresponding element mapping images. Purple, yellow, and green represent Ag, C, and O elements, respectively. (i) Cryo-HRTEM image of the discharge cathode. (j) The local magnification acquired from the boxed regions in (i). (k) Cryo-HRTEM image of the discharge cathode. ((l) and (m)) The local magnification of areas III and IV in (k), respectively. ((n) and (o)) The corresponding FFT patterns of (l) and (m), respectively. (p) Cryo-TEM image and ((q) and (r)) the IFFT patterns of the local magnification images of regions V and VI in (p), respectively. (s) Atomic resolution HAADF image of the discharge product and ((t) and (u)) the enlarged view of regions VII and VIII in (s), respectively. (v) Reaction-free energy diagrams of the discharge process on the Ag and Li-Ag alloy models. ((w) and (x)) Optimized structures and the intermediates adsorption under the discharge of Li-CO_2 battery on Ag and Li-Ag alloy models, respectively.

ESM) and the magnified images (Figs. 3(t) and 3(u), and Figs. S12(b) and S12(f) in the ESM) with the corresponding FFT patterns (Figs. S12(c), S12(d), S12(g), S12(h), and S13(a)–S13(d) in the ESM) of the nanoparticles in the film layer confirm that the nanoparticles are $LiAg_3O_2$ (JCPDS No. 70-1743) along the [111], [001], [142], and [$3\bar{1}\bar{1}$] zone axes, and the structural models (Figs. S14(a)–S14(d) in the ESM) fit well with the HAADF-STEM images. Moreover, HAADF-STEM images (Figs. S15(a)–S15(d) in the ESM) further show the highly dispersed NPs with a significant number of atomic clusters and single atoms, which may act as important catalytic sites for the CRR and CER. The Cryo-TEM and the magnified images as well as the corresponding FFT patterns (Figs. S16(a)–S16(c) and S17(a)–S17(c) in the ESM) reveal the interface structure between the Ag NWs and the discharge products, indicating that the $LiAg_3O_2$ NPs are uniformly dispersed in the Li_2CO_3 and a-C matrix layer. The clearly observed three-phase interfaces (arrows in Fig. S18 in the ESM) among $LiAg_3O_2$, Li_2CO_3, and a-C indicate the critic catalytic effect of Li-Ag alloy on the formation of discharge products of Li_2CO_3 and a-C. Part of the Li-Ag alloy transforms to $LiAg_3O_2$ during the discharge process via the oxidation of Li-Ag alloy by the CO_2. The three-phase interfaces (arrow in Fig. S19 in the ESM) far from the Ag NW surface confirm that the *in-situ* formed Li-Ag alloy rather than the Ag plays the dominant role in the discharge process of the ASS Li-CO_2 batteries.

Density functional theory (DFT) calculation was performed to explore the thermodynamics of the CRR. As shown in Figs. 3(v)–3(x), we performed the optimization of discharge product structures and adsorption sites of intermediates under Li-Ag alloy(110) and Ag(110) surface models, as well as calculated the reaction free energies for the CRR processes on Li-Ag alloy and Ag catalyst surfaces. The reaction path for the generation of Li_2CO_3 are divided into seven steps [44, 45].

$$Li^+ + CO_2 + e^- + * \rightarrow LiCO_2* \quad (I)$$

$$LiCO_2* + CO_2 \rightarrow LiCO_3* + CO* \quad (II)$$

$$LiCO_3* + CO* + Li^+ + e^- \rightarrow Li_2CO_3* + CO* \quad (III)$$

$$Li_2CO_3* + CO* \rightarrow Li_2CO_3 + CO* \quad (IV)$$

$$CO* + CO_2 \rightarrow CO_3* + C* \quad (V)$$

$$CO_3* + C* + Li^+ + e^- \rightarrow LiCO_3* + C* \quad (VI)$$

$$LiCO_3* + C* + Li^+ + e^- \rightarrow Li_2CO_3* + C* \quad (VII)$$

The process of steps (I)–(III) in the reaction free energy diagram involves the formation of intermediate $LiCO_2*$ with CO_2 to form a $LiCO_3*$ intermediate, which then reacts with Li^+ to generate Li_2CO_3*. In step (IV), the energy barrier for the transformation of adsorbed intermediate Li_2CO_3* to Li_2CO_3 over the Li-Ag alloy catalyst is 1.50 eV. The formation of CO_3* and C* is the rate-determining step of the whole reaction, corresponding to step (V) in the reaction free energy diagram. Here, the reaction free energy for step (V) on Li-Ag alloy catalyst (−3.36 eV) is much lower than that on Ag catalyst (3.25 eV). Subsequently, the intermediate CO_3* reacts with Li^+ to generate the Li_2CO_3* species (steps (VI) and (VII)). Notably, the atomic arrangement of Li-Ag alloy surface model undergoes significant disruption during the step (V) of discharge process, which is attributed to the oxidation of the Li-Ag alloy to form $LiAg_3O_2$, consistent with the HRTEM image (Fig. S20 in the ESM) showing that $LiAg_3O_2$ NPs consistently detach from the Ag NWs and uniformly disperse in the Li_2CO_3 and a-C matrix layer. These results indicate that compared with Ag, Li-Ag alloy exhibits higher catalytic propensity for the formation of Li_2CO_3 and a-C, corresponding to the Li_2CO_3* and C* in step (VII). However, the Li-Ag alloy catalyst undergoes irreversible structural rearrangement and oxidization to form $LiAg_3O_2$, which is one of the factors contributing to the poor cycling performance of the ASS Li-CO_2 battery. Both experimental data and DFT calculations underscore that the *in-situ* formed Li-Ag alloy serves as efficient catalysts in Li-CO_2 batteries, exhibiting excellent catalytic effect for CO_2 reduction at Li-Ag alloy sites.

After charging, Cryo-TEM images and the corresponding enlarged images (Figs. 4(a)–4(c) and Figure S21(a)–S21(c) in the ESM) indicate the decomposition of the discharge product coated on the Ag NWs although some residue still remains. Based on the analysis of Raman spectrum (Fig. 2(f)), EDPs (Fig. 4(d)), and EELS (Figs. 4(f) and 4(g)), Li_2CO_3 decomposes after charging. However, both XRD (Fig. 2(g)) and EDPs (Fig. 4(e)) indicate that a small amount of undecomposed Li_2CO_3 residues still exist after charging in the areas with relatively thick the film-like discharge products. The HRTEM (Fig. 4(h)) and the corresponding magnified images (Figs. 4(i)–4(k)) of the products after charging are indexed as $LiAg_3O_2$, a-C, and a small amount of residual Li_2CO_3. As shown in Fig. S22 in the ESM, the Coulombic efficiency calculated from the discharge/charge curve is 28.99%. The accumulation of a-C layer and a small amount of undecomposed Li_2CO_3 slow down Li ion diffusion and hinder gas permeation, resulting in irreversible capacity loss of the ASS Li-CO_2 battery. The a-C deposition in Ag NWs also increases the impedance of the battery with increasing discharge/charge cycle, as shown in the EIS before and after cycling (Fig. 2(e)).

The comparison of Cryo-TEM images of the cathode catalysts after discharge and charge demonstrates significant size and shape change of Ag NWs. After discharge, the average diameter of the Ag NWs is 30.8 ± 6.1 nm, with a mean length of 2.5 ± 0.7 μm (Figs. S23(e)–S23(h) in the ESM), which is narrower and shorter than those of the pristine Ag NWs (average diameter of 31.9 ± 6.4 nm and mean length of 10.2 ± 0.2 μm in Figs. S23(a)–S23(d) in the ESM). The charged Ag NWs reduce the mean diameter size to 29.3 ± 5.2 nm, and the average length to 398 ± 246 nm (Figs. S23(i)–S23(l) in the ESM), displaying a relatively narrower and shorter distribution than that of the Ag NWs after both discharge and charge. These results indicate that Ag NWs are consumed during both discharging and charging, which could be attributed to that the Ag catalyst facilitates the decomposition of Li_2CO_3, which is oxidized into $LiAg_2O_3$ and thereby further consumes during the charging process. To verify this hypothesis, we investigated the Li_2CO_3 decomposition process catalyzed by Ag via DFT calculations.

In the case of CER, we performed the optimization of charge product structures and adsorption sites of intermediates under model of Ag(110) surface, and calculated the reaction free energies for ASS Li-CO_2 battery charge process on Ag catalyst surfaces using DFT (Figs. 4(l) and 4(m)). As illustrated in the steps (2) and (3), Li_2CO_3* first breaks the Li–O bond to form $LiCO_3$–Li*, and then

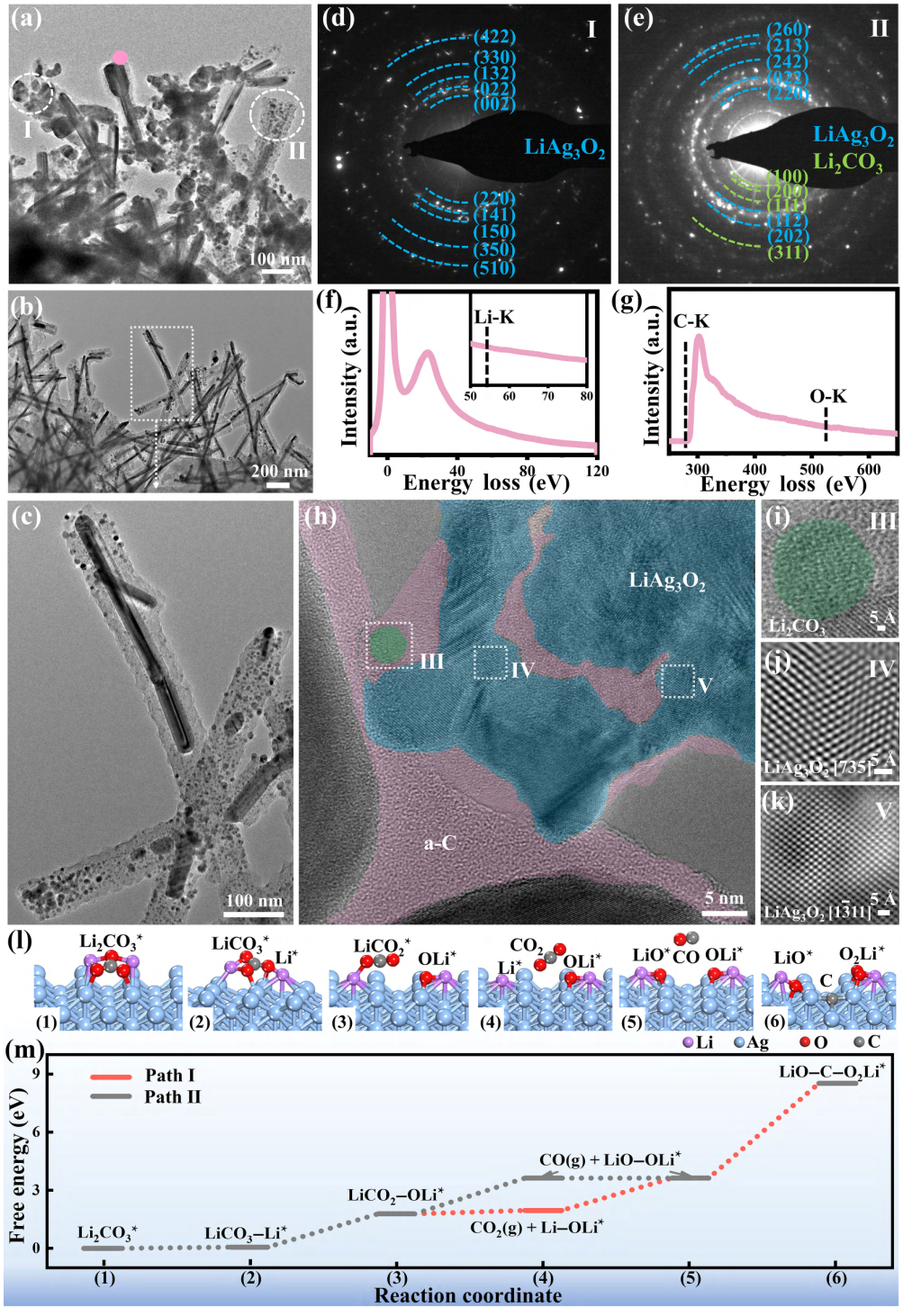

Figure 4 Electron microscopy characterizations of the charge products and DFT calculations of the CER thermodynamics. (a) Cryo-TEM image of the charge products. (b) Cryo-TEM image and (c) the corresponding enlarged view of the charge products. ((d) and (e)) EDPs acquired from circular regions I and II in (a). (f) Low-loss and (g) core-loss EELS spectra of the charge products (pink in (a)). (h) Cryo-HRTEM image of the charge Ag cathode catalyst and ((i)–(k)) local magnification of areas I–III, respectively. (l) Optimized adsorption geometries of Li_2CO_3 on Ag surfaces. (m) Reaction-free energy diagrams of the charge process on the Ag model.

breaks the C–O bond in $LiCO_3$-Li* to form $LiCO_2$–OLi*. Next, the decomposition process branches into wo pathways

$$Li_2CO_3^* \rightarrow LiCO_3 - Li^* \rightarrow LiCO_2 - OLi^* \rightarrow CO_2(g) + Li - OLi^* \rightarrow CO(g) + LiO - OLi^* \rightarrow LiO - C - O_2Li^* \quad \text{(path I)}$$

$$Li_2CO_3^* \rightarrow LiCO_3 - Li^* \rightarrow LiCO_2 - OLi^* \rightarrow CO(g) + LiO - OLi^* \rightarrow LiO - C - O_2Li^* \quad \text{(path II)}$$

In path I, the $LiCO_2$* intermediate breaks the Li–O bond to form CO_2. In path II, the $LiCO_2$* intermediate breaks the C–O bond to form CO. Additionally, the transition from step (3) directly to step (5) requires crossing a considerably high energy barrier.

Subsequently, CO_2 and CO are adsorbed on the Ag surface and reduced to C in paths I and II, respectively, and both of these processes require greater energy. Clearly, the energy required to form CO_2 is lower. The results indicate that Li_2CO_3 decomposes into CO_2 during the charging process, and the charging capacity is mainly provided by the oxidation of Ag. Moreover, additional $LiAg_3O_2$ also forms during the charge process, and the OLi* intermediate is adsorbed on the surface of Ag and eventually evolves into $LiAg_3O_2$, which is consistent with the results revealed by Cryo-TEM (Figs. S24(a)–S24(c) in the ESM). The decomposition of Li_2CO_3 occurs, while a-C does not participate in the CER reaction, causing the accumulation of carbon. In addition, Ag catalyst is further consumed during CER process, making it difficult for Li_2CO_3 far from Ag NWs to decompose, thereby leading to poor cycling performance of the ASS Li-CO_2 battery.

To verify the microstructure evolution and the phase transformation of Ag NWs cathode catalysts during discharge–charge process, an *in-situ* TEM characterization was conducted in an ASS Li-CO_2 nanobattery. The Li-CO_2 nanobattery was constructed with two probes (Al tip and Cu grid), as shown in Fig. S25(a) in the ESM. The Ag NWs glued to the Cu grid were used as the cathode catalyst for CO_2 electrode. The bulk Li coated on the Al tip served as the counter electrode. The *in-situ* formed Li_2CO_3/Li_2O composite on the Li metal was used as solid state electrolyte for Li-CO_2 nanobattery, and an CO_2 gas environment in ETEM with a constant pressure of 1.0 mbar was maintained around the nanobattery cell during the experiments. Using this setup, the electrons and Li^+ produced in electrochemical charge/discharge reactions would transfer only through the Ag NWs. As a result, Li^+, electrons, and CO_2 will react at Ag NWs during the discharge reaction. When an appropriate operating potential was applied to the Li-CO_2 nanobattery, the discharge/charge processes can be visualized in real-time, and the discharge-induced structural and morphological evolution were obtained.

Morphology and structure evolution of the Ag NW cathode during discharge and charge were analyzed by *in-situ* TEM images, EDPs, and EELS. Upon applying a negative potential to the Ag NW against Li anode, the discharge products are present on the surface of Ag NWs, and the consumption of Ag NW occurs (Figs. 5(a)–5(d) and Movie S1 in the ESM). As shown in Fig. 5(g), the Ag is lithiated to form $Li_{33.44}Ag_{18.56}$ alloy. The diffraction rings in the EDPs of the discharge product (Fig. 5(h)) and the corresponding integral intensity of diffraction pattern (Fig. 5(k)) can be indexed as $LiAg_3O_2$ and Li_2CO_3. The nanobattery was recharged by applying a reverse bias (Figs. 5(e) and 5(f)). After charging, the diameter and lengths of the Ag NW further decrease (Figs. S25(b)–S25(f) and Movie S2 in the ESM). It is found that the diffraction rings in the EDPs (Fig. S25(g) in the ESM) of the discharge product can be indexed as LiAg, $LiAg_3O_2$, and Li_2CO_3. These phenomena indicate that the Ag NW is further consumed during the charging process. The EDPs (Figs. 5(i) and 5(j), and Fig. S25(h) in the ESM) and the corresponding diffraction pattern integral (Fig. 5(l)) of the charge product indicate that the final product is $LiAg_3O_2$ and trace residual Li_2CO_3. The low-loss EELS spectrum (Fig. 5(m)) of the discharge product shows a peak around 55 eV, which corresponds to the Li-K edge. The core-loss EELS (Fig. 5(o)) peaks at 284 and 532 eV correspond to the C-K and O-K edges, respectively, and all these peaks are consistent with the EELS profile of Li_2CO_3 [46]. The EELS analysis (Figs. 5(n) and 5(p)) show that only the C-K edge presents in the low-loss and core-loss EELS spectra after charging, indicating that the a-C residue remains after the decomposition of Li_2CO_3 during charging [47]. According to *in-situ* TEM experiments (Figs. S26(a)–S26(h) and S27(a)–S27(k), and Movies S3–S5 in the ESM), Li-Ag alloy is firstly formed in the Li-CO_2 nanobattery during discharge process, which acts as an efficient catalyst in the CRR, and then the discharge products Li_2CO_3 and a-C appear with the formation of intermediate $LiAg_3O_2$. The visualization of a-C accumulation on the Ag NWs during the oxidation process, as well as the irreversible consumption of Ag catalysts, clearly reveals the failure mechanism of ASS Li-CO_2 nanobatteries. These *in-situ* observations are consistent with the experimental results obtained in the macroscopic ASS Li-CO_2 batteries.

To summarize the reaction and failure mechanisms of the ASS Li-CO_2 batteries, a schematic diagram of the relevant mechanisms is shown in Fig. 6. The discharge process can be described by the following two steps: The Li-Ag alloy is *in-situ* formed by the alloying of Ag with electrochemical plated Li via reaction (1)

$$Ag + xLi^+ + xe^- \rightarrow Li_xAg \quad (1)$$

and CO_2 reacts with highly dispersed Li atoms in the Li-Ag alloy and electrons via reaction (2)

$$3Li_xAg + (5-3x)Li^+ + 4CO_2 + (5-3x)e^- \rightarrow 2Li_2CO_3 + LiAg_3O_2 + 2C \quad (2)$$

The discharge products of $LiAg_3O_2$ nanoparticles uniformly disperse in Li_2CO_3 and a-C. During charge, the Ag NWs are further consumed to catalyze the decomposition of Li_2CO_3. The Ag is oxidized to form $LiAg_3O_2$, while the Li_2CO_3 is only chemically decomposed to form Li^+ and CO_2 via reaction (3)

$$3Ag + 2Li_2CO_3 \rightarrow LiAg_3O_2 + 2CO_2 + 3Li^+ + 3e^- \quad (3)$$

causing the residual a-C to aggregate and form a visible shell on the Ag NWs, both of which isolate the Ag NWs with the CO_2 gas, thus shuts off the CRR/CER, causing the failure of the ASS Li-CO_2 batteries.

3 Conclusions

The reaction and failure mechanisms of the ASS Li-CO_2 batteries were investigated by constructing LLZTO ASS electrolyte and 3D Ag NWs framework cathode catalysts without the interference of binder, carbon-based catalysts, and liquid electrolytes. Cryo-TEM images and DFT calculations demonstrate that the Li-Ag alloy *in-situ* forms first, and then numerous $LiAg_3O_2$ NPs are emerge in the film-like Li_2CO_3 and a-C product layer under the catalysis of Li-Ag alloy during CO_2 reduction process. Subsequently, the Ag NWs are irreversibly consumed to catalyze the decomposed of Li_2CO_3 at a low charge potential of ~ 3.5 V, and CO_2 fixation is achieved through the accumulation of a-C during charge. Li-CO_2 nanobatteries were assembled in an ETEM, showing that the irreversible consumption of the active Ag catalysts and the continuous accumulation of the a-C layer shut off the electrochemical reactions, thereby directly confirming the reaction and failure mechanisms of ASS Li-CO_2 battery. In a broader perspective, we believe that the fundamental insights into the electrochemistry of ASS Li-CO_2 battery presented in this study provide strong scientific basis for the development of CO_2 fixation and CO_2-based energy storage systems.

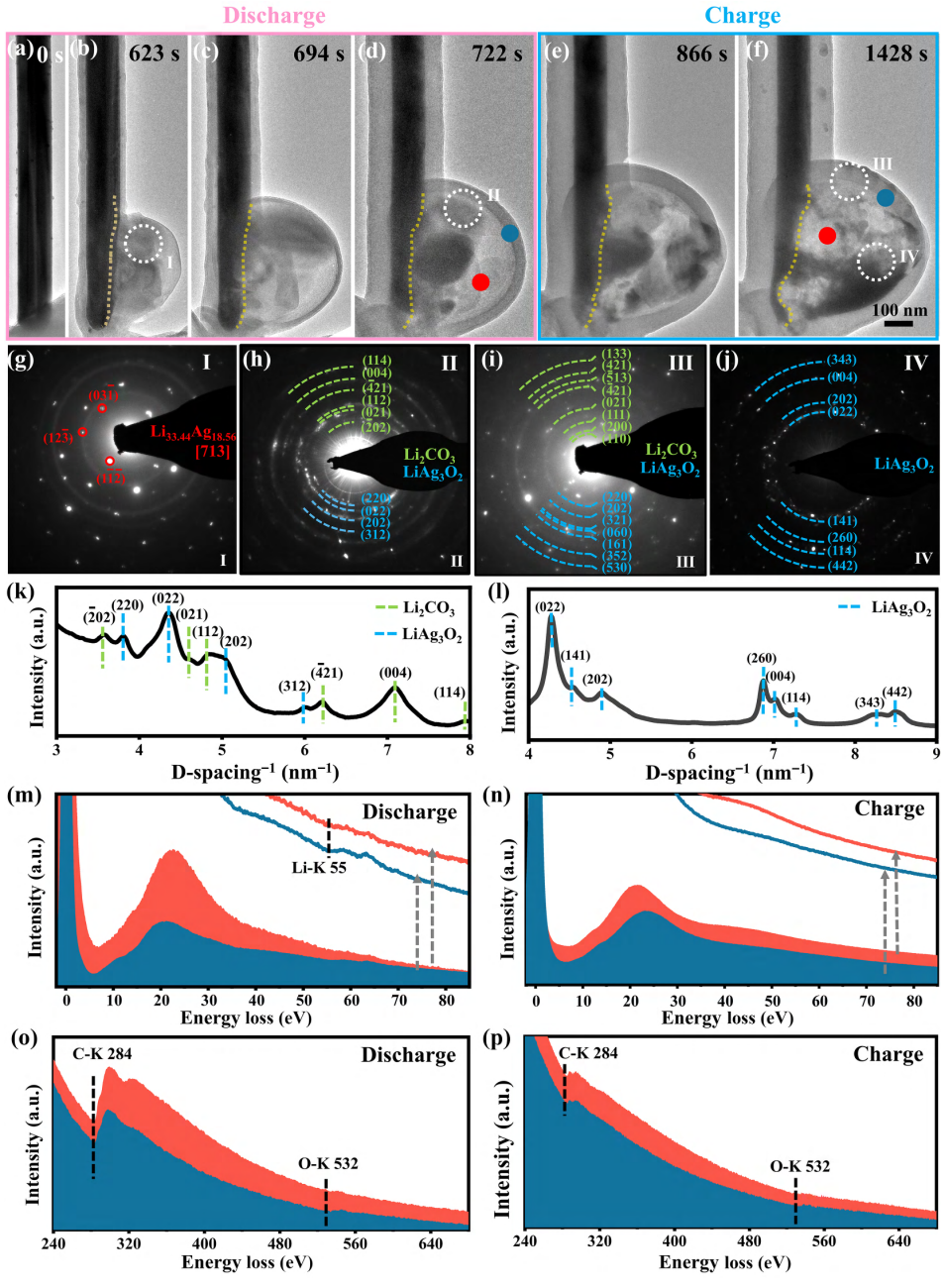

Figure 5 Structure evolutions of the Ag NWs after discharge and charge processes of a Li-CO_2 nanobattery. ((a)–(f)) Time-lapse morphological evolution of Ag NWs in an Li-CO_2 nanobattery during the discharge and charge process. ((g) and (h)) The EDPs of the product after discharging from regions outlined by circles I and II in (b) and (d), respectively. ((i) and (j)) The EDPs of the product after charging from regions outlined by circles III and IV in (f), respectively. ((k) and (l)) The diffraction integrals of (h) and (j), respectively. ((m) and (n)) The Low-loss and ((o) and (p)) core-loss EELS of the discharge (red and blue in (d)) and charge (red and blue in (f)) products, respectively.

4 Experimental

4.1 Material preparation

The garnet-type LLZTO solid electrolytes (12 mm in diameter and 1 mm in thickness) were prepared via solid-state reactions as reported previously [48]. The obtained LLZTO pellets had a relative density of 99.6%. The nanometer Au on the LLZTO pellets was prepared by ion sputtering technology (ISC-200) at a sputtering current of 15 mA. For the ~ 80 nm-thick Au layer sample, the sputtering time was 10 s with 5 deposition cycles. For the ~ 160 nm-thick Au layer sample, the sputtering time was 10 s with 10 deposition cycles. The Ag NW dispersions were customized from Nano Chemical Technology Company (a purity of 99.9%, a diameter of ~ 33 nm, a length of 10 μm, and a concentration of 5 mg·mL^{-1}). MWCNTs were purchased from Macklin.

4.2 Battery assembly and test

Ag NW cathode catalysts were fabricated by spin-coating the Ag NW dispersion on the LLZTO ceramic pellets, and the Au layers were coated on the LLZTO pellets. The 3D framework of Ag NWs formed on the LLZTO pellets was subsequently dried in a vacuum

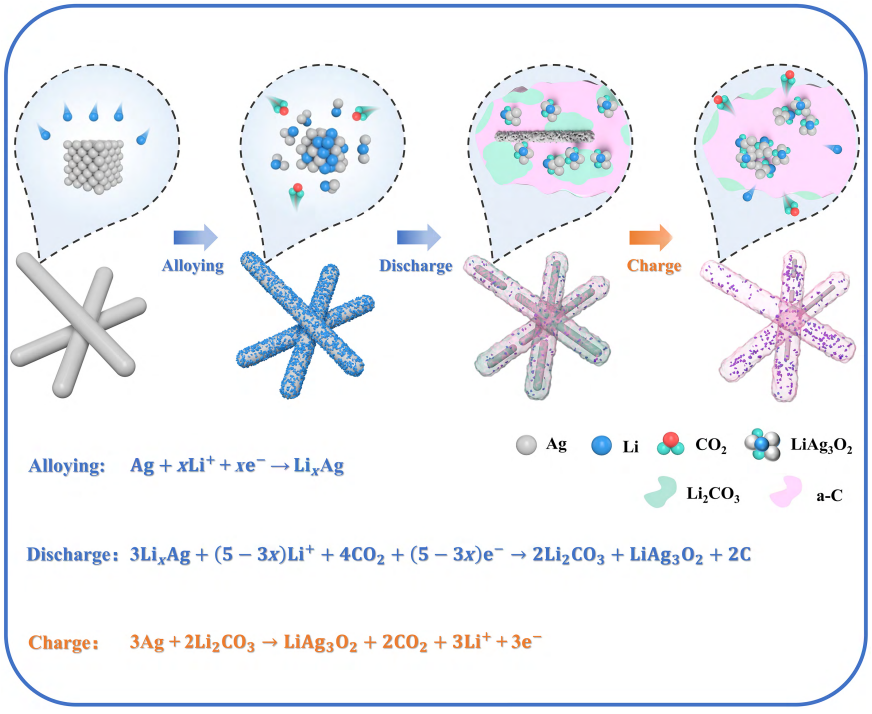

Figure 6 Schematic illustration of the proposed reaction and failure mechanisms of all-solid-state Li-CO_2 batteries.

chamber at 100 °C for 12 h. To avoid moisture attack during the experiments, all the cells were assembled in an Ar-filled glovebox with H_2O and O_2 less than 0.1 ppm. The Li anodes were prepared by pressing Li foils (a diameter of 11 mm and a thickness of 0.5 mm) onto the opposite side of LLZTO. After being integrated into the Swagelok-type and sealed in homemade cell containers, the cells were put inside a chamber of 80 °C and then flushed with pure CO_2 for battery testing. A LAND CT3001A battery test system was used for the electrochemical measurements of the Li-CO_2 batteries.

4.3 Nanobattery testing

The charge/discharge reactions of Ag NWs were investigated in a Li-CO_2 nanobattery by using an ETEM (FEI-Titan G2 ETEM, 300 kV). A few drops of ultrasonic dispersed Ag NWs were casted on the aluminum tip as the cathodes. In a glove box filled with Ar atmosphere, metal Li scratched on a tungsten (W) tip was used as the anode. The nanobattery was assembled in a TEM-scanning tunneling microscopy (TEM-STM) sample rod (Pico Femto FE-F20), then placed in Ar dry airtight bag and transferred into a Cs-corrected ETEM. During the process of charge/discharge, at a pressure of 1 mbar, CO_2 gas (purity was higher than 99.99%) was flowed into the specimen chamber. The Ag NW was manipulated to approach the Li layer, and then a potential was applied to the nanowire versus the Li metal electrode to either charge or discharge the nanobattery.

4.4 Characterizations

Raman spectra were obtained with a 532 nm wavelength laser using a Renishaw inVia system. The surface chemistry of the samples was examined using an XPS (Thermo Scientific K-Alpha) spectrometer with a vacuum transfer equipment. XRD was carried out using a Rigaku D/MAX-2500/PC (Cu Kα) at 5 °·min^{-1} over a 2θ range of 25–45°. The samples were not exposed to air from preparation to testing. Surface morphology study and element mapping were performed using SEM (FEI, FIB-Helios G4 Cx, Thermo fisher scientific). The samples were put in the home-made sample transfer device with a lid that could be opened and closed in the glove box, which avoided air exposure of samples during transfer process. Then, the device with the sample was transferred to SEM, and the lid was opened for sample processing and characterization. The TEM images were acquired in an ETEM (Titan G2, Thermo Fisher Scientific) with a Gatan EELS system (GIF-Quantum 965 spectrometer) at 300 kV. Electron dose rate was kept at the minimum in order to minimize electron beam induced sample damage. The TEM grid with the discharge/charge products was subjected to a liquid nitrogen (L-N_2) bath connected to the cooling holder, then loaded onto the cryo transfer holder (FISCHIONE, Model 2550) and sealed with a shutter in L-N_2, and transferred into TEM chamber. The samples could be cooled down to about −173 °C. The HAADF-STEM and STEM-EDS measurements were performed in a TEM (Talos F20, Thermo Fisher Scientific) at 200 kV. The collection semi-angle of the STEM detectors was set to 41–200 mrad for HAADF imaging.

All DFT calculations were performed by using Vienna *ab-initio* simulation package (VASP). The DFT functional was utilized at the Perdew–Burke–Ernzerhof level [49–51]. The plane wave basis set kinetic energy cutoff was set to 450 eV [52, 53]. The electronic energy was considered self-consistent when the energy change was smaller than 10^{-5} eV. The force thresholds of 0.05 eV·Å^{-1} were used for the structure optimization of all intermediates. During the relaxation, the Brillouin zone with a 4 × 4 × 1 Gamma centered grid was used. For each elementary step, the Gibbs reaction free energy ΔG is defined as the difference between free energies of the initial and final states and is given by the expression

$$\Delta G = \Delta E + \Delta ZPE - T\Delta S \quad (4)$$

where ΔE is the reaction energy of reactant and product molecules adsorbed on catalyst surface obtained from DFT calculations, ΔZPE

is the difference of zero-point energy, T is the temperature (298.15 K), and ΔS is the change in the entropy. The zero-point energy and entropy were obtained through vibrational frequencies.

Electronic Supplementary Material: Supplementary material (SEM, Cryo-TEM, HAADF-STEM, and *in-situ* TEM characterizations of the discharge/charge products; Movies S1–S5) is available in the online version of this article at https://doi.org/10.26599/NR.2026.94908658.

Data availability

All data needed to support the conclusions in the paper are presented in the manuscript and the Electronic Supplementary Material. Additional data related to this paper may be requested from the corresponding author upon request.

Acknowledgements

This work was financially supported by the National Natural Science Foundation of China (Nos. 22279112, 22579145, 51772262, 5197010923, 51971245, 52002346, 52022088, U20A20336, 21935009, and 22408146), Natural Science Foundation of Hebei Province (Nos. B2023203031, B2022203018, B2018203297, B2024203054, and F2021203097), Fundamental Research Specialized Program of Higher Education in Hebei Province (No. JCZX2025013), Key Research and Development Program Projects of Shandong Province (No. 2024TSGC0915), Taishan Industrial Experts Program, Hebei One Hundred Talent Program (No. 4570028), High-Level Talents Research Program of the Yanshan University (Nos. 00500021502 and 005000201), Hebei Key Laboratory of Applied Chemistry after Operation Performance (No. 22567616H), and Science and Technology Innovation Program of Hunan Province (No. 2021RC3109).

Declaration of competing interest

All the contributing authors report no conflict of interests in this work.

Author contribution statement

Z. Y. G.: Project administration, writing manuscript, experimental design. H. X.: Data curation, validation, experimental design. Q. S. D.: Data curation. Y. L. L.: Data curation, validation. R. H. Z.: Data curation. B. W.: validation. Z. Y. R.: validation. J. Y. L.: Data curation. A. L. B.: Data curation. J. C. C.: Validation. W. L.: Project administration. H. L. Q.: Project administration. F. H.: Project administration. J. Z. C.: Project administration, funding acquisition, writing manuscript. Y. F. T.: Project administration, funding acquisition, writing manuscript. J. Y. H.: Project administration, funding acquisition, writing manuscript. All the authors have approved the final manuscript.

Use of AI statement

None.

References

[1] Schrag, D. P. Preparing to capture carbon. *Science* **2007**, *315*, 812–813.

[2] Matter, J. M.; Stute, M.; Snæbjörnsdottir, S. Ó.; Oelkers, E. H.; Gislason, S. R.; Aradottir, E. S.; Sigfusson, B.; Gunnarsson, I.; Sigurdardottir, H.; Gunnlaugsson, E. et al. Rapid carbon mineralization for permanent disposal of anthropogenic carbon dioxide emissions. *Science* **2016**, *352*, 1312–1314.

[3] Al Sadat, W. I.; Archer, L. A. The O_2-assisted Al/CO_2 electrochemical cell: A system for CO_2 capture/conversion and electric power generation. *Sci. Adv.* **2016**, *2*, e1600968.

[4] Li, X.; Yang, S. X.; Feng, N. N.; He, P.; Zhou, H. S. Progress in research on Li-CO_2 batteries: Mechanism, catalyst and performance. *Chin. J. Catal.* **2016**, *37*, 1016–1024.

[5] Weng, Z.; Jiang, J. B.; Wu, Y. S.; Wu, Z. S.; Guo, X. T.; Materna, K. L.; Liu, W.; Batista, V. S.; Brudvig, G. W.; Wang, H. L. Electrochemical CO_2 reduction to hydrocarbons on a heterogeneous molecular Cu catalyst in aqueous solution. *J. Am. Chem. Soc.* **2016**, *138*, 8076–8079.

[6] Xu, S. M.; Das, S. K.; Archer, L. A. The Li-CO_2 battery: A novel method for CO_2 capture and utilization. *RSC Adv.* **2013**, *3*, 6656–6660.

[7] Liu, B.; Sun, Y. L.; Liu, L. Y.; Chen, J. T.; Yang, B. J.; Xu, S.; Yan, X. B. Recent advances in understanding Li-CO_2 electrochemistry. *Energy Environ. Sci.* **2019**, *12*, 887–922.

[8] Zou, J. S.; Gupta, D.; Yuwono, J. A.; Zhang, S. L.; Guo, Z. P. The promises and reality of metal-CO_2 batteries. *Nat. Rev. Clean Technol.* **2025**, *1*, 699–718.

[9] Mu, X. W.; He, P.; Zhou, H. S. Toward practical Li-CO_2 batteries: Mechanisms, catalysts, and perspectives. *Acc. Mater. Res.* **2024**, *5*, 467–478.

[10] Ma, W. Q.; Jian, T. Z.; Wang, Y. Y.; Ma, J. P.; Gao, H. Y.; Li, X. H.; Liu, S. Y.; Gao, M. J.; Chen, X. P.; Yang, L. S. et al. Pathway engineering in Li-CO_2 batteries: Mitigating energy barriers via optimized $4e^-/3CO_2$ and $2e^-/2CO_2$ redox chemistry. *Adv. Funct. Mater.*, in press, DOI: 10.1002/adfm.202524344.

[11] Yang, T. T.; Li, H.; Chen, J. Z.; Ye, H. J.; Yao, J. M.; Su, Y. W.; Guo, B. Y.; Peng, Z. Q.; Shen, T. D.; Tang, Y. F. et al. *In situ* imaging electrocatalytic CO_2 reduction and evolution reactions in all-solid-state Li-CO_2 nanobatteries. *Nanoscale* **2020**, *12*, 23967–23974.

[12] Du, Y. M.; Liu, Y. J.; Yang, S. X.; Li, C.; Cheng, Z.; Qiu, F. L.; He, P.; Zhou, H. S. A rechargeable all-solid-state Li-CO_2 battery using a $Li_{1.5}Al_{0.5}Ge_{1.5}(PO_4)_3$ ceramic electrolyte and nanoscale RuO_2 catalyst. *J. Mater. Chem. A* **2021**, *9*, 9581–9585.

[13] Xiao, S. S.; Xiao, Y.; He, G.; Zhang, T. H.; Yang, L. L.; Huo, F.; Chen, S. M. Synergistic Cu-based catalysts with multiple active sites for high-efficiency Li-CO_2 batteries. *Chem. Sci.* **2025**, *16*, 17640–17648.

[14] Sun, L.; Yuwono, J. A.; Zhang, S. L.; Chen, B.; Li, G. J.; Jin, H. Y.; Johannessen, B.; Mao, J. F.; Zhang, C. F.; Zubair, M. et al. High entropy alloys enable durable and efficient lithium-mediated CO_2 redox reactions. *Adv. Mater.* **2024**, *36*, 2401288.

[15] Sun, L.; Wen, K. H.; Li, G. J.; Zhang, X. D.; Zeng, X. H.; Johannessen, B.; Zhang, S. L. High-entropy alloys in catalysis: Progress, challenges, and prospects. *ACS Mater. Au* **2024**, *4*, 547–556.

[16] Qiao, Y.; Yi, J.; Wu, S. C.; Liu, Y.; Yang, S. X.; He, P.; Zhou, H. S. Li-CO_2 electrochemistry: A new strategy for CO_2 fixation and energy storage. *Joule* **2017**, *1*, 359–370.

[17] Liu, Y. Q.; Mao, R.; Chen, B.; Lu, B. Y.; Piao, Z.; Song, Y. Z.; Zhou, G. M.; Cheng, H. M. Atomic design of bidirectional electrocatalysts for reversible Li-CO_2 batteries. *Mater. Today* **2023**, *63*, 120–136.

[18] Chen, K.; Yang, D. Y.; Huang, G.; Zhang, X. B. Lithium-air batteries: Air-electrochemistry and anode stabilization. *Acc. Chem. Res.* **2021**, *54*, 632–641.

[19] Chen, J.; Chen, X. Y.; Liu, Y.; Qiao, Y.; Guan, S. Y.; Li, L.; Chou, S. L. Recent progress of transition metal-based catalysts as cathodes in O_2/H_2O-involved and pure Li-CO_2 batteries. *Energy Environ. Sci.* **2023**, *16*, 792–829.

[20] Liu, Y. Q.; Zhang, Z. Y.; Tan, J. Y.; Chen, B.; Lu, B. Y.; Mao, R.;

Liu, B. L.; Wang, D. S.; Zhou, G. M.; Cheng, H. M. Deciphering the contributing motifs of reconstructed cobalt(II) sulfides catalysts in Li-CO_2 batteries. *Nat. Commun.* **2024**, *15*, 2167.

[21] Lu, B. Y.; Wu, X. R.; Zhang, M. T.; Xiao, X.; Chen, B.; Liu, Y. Q.; Mao, R.; Song, Y. Z.; Zeng, X. X.; Yang, J. L. et al. Steering the orbital hybridization to boost the redox kinetics for efficient Li-CO_2 batteries. *J. Am. Chem. Soc.* **2024**, *146*, 20814–20822.

[22] Chen, B.; Wang, D. S.; Tan, J. Y.; Liu, Y. Q.; Jiao, M. L.; Liu, B. L.; Zhao, N. Q.; Zou, X. L.; Zhou, G. M.; Cheng, H. M. Designing electrophilic and nucleophilic dual centers in the ReS_2 plane toward efficient bifunctional catalysts for Li-CO_2 batteries. *J. Am. Chem. Soc.* **2022**, *144*, 3106–3116.

[23] Zhang, P. F.; Zhang, J. Y.; Sheng, T.; Lu, Y. Q.; Yin, Z. W.; Li, Y. Y.; Peng, X. X.; Zhou, Y.; Li, J. T.; Wu, Y. J. et al. Synergetic effect of Ru and NiO in the electrocatalytic decomposition of Li_2CO_3 to enhance the performance of a Li-CO_2/O_2 battery. *ACS Catal.* **2020**, *10*, 1640–1651.

[24] Li, S. W.; Dong, Y.; Zhou, J. W.; Liu, Y.; Wang, J. M.; Gao, X.; Han, Y. Z.; Qi, P. F.; Wang, B. Carbon dioxide in the cage: Manganese metal-organic frameworks for high performance CO_2 electrodes in Li-CO_2 batteries. *Energy Environ. Sci.* **2018**, *11*, 1318–1325.

[25] Zhang, X.; Wang, X. G.; Xie, Z. J.; Zhou, Z. Recent progress in rechargeable alkali metal-air batteries. *Green Energy Environ.* **2016**, *1*, 4–17.

[26] Xie, Z. J.; Zhang, X.; Zhang, Z.; Zhou, Z. Metal-CO_2 batteries on the road: CO_2 from contamination gas to energy source. *Adv. Mater.* **2017**, *29*, 1605891.

[27] Peng, Z. Q.; Freunberger, S. A.; Hardwick, L. J.; Chen, Y. H.; Giordani, V.; Bardé, F.; Novak, P.; Graham, D.; Tarascon, J. M.; Bruce, P. G. Oxygen reactions in a non-aqueous Li^+ electrolyte. *Angew. Chem., Int. Ed.* **2011**, *50*, 6351–6355.

[28] Zhang, Z.; Zhang, Q.; Chen, Y. N.; Bao, J.; Zhou, X. L.; Xie, Z. J.; Wei, J. P.; Zhou, Z. The first introduction of graphene to rechargeable Li-CO_2 batteries. *Angew. Chem., Int. Ed.* **2015**, *54*, 6550–6553.

[29] Zhang, Z.; Wang, X. G.; Zhang, X.; Xie, Z. J.; Chen, Y. N.; Ma, L. P.; Peng, Z. Q.; Zhou, Z. Verifying the rechargeability of Li-CO_2 batteries on working cathodes of Ni nanoparticles highly dispersed on N-doped graphene. *Adv. Sci.* **2018**, *5*, 1700567.

[30] Ahmadiparidari, A.; Warburton, R. E.; Majidi, L.; Asadi, M.; Chamaani, A.; Jokisaari, J. R.; Rastegar, S.; Hemmat, Z.; Sayahpour, B.; Assary, R. S. et al. A long-cycle-life lithium-CO_2 battery with carbon neutrality. *Adv. Mater.* **2019**, *31*, 1902518.

[31] Yang, S. X.; He, P.; Zhou, H. S. Exploring the electrochemical reaction mechanism of carbonate oxidation in Li-air/CO_2 battery through tracing missing oxygen. *Energy Environ. Sci.* **2016**, *9*, 1650–1654.

[32] Zhang, X.; Zhang, Q.; Zhang, Z.; Chen, Y. N.; Xie, Z. J.; Wei, J. P.; Zhou, Z. Rechargeable Li-CO_2 batteries with carbon nanotubes as air cathodes. *Chem. Commun.* **2015**, *51*, 14636–14639.

[33] Gao, Z. S.; Yang, S. J.; Yang, Y.; Sun, F. T.; Zhang, T. S.; Wang, Y. L.; Zhou, T. R.; Tao, L.; Song, H. C.; Chen, H. J. A three-in-one strategy enables improved kinetics in an LLZTO solid electrolyte for Li-CO_2 batteries with high energy efficiency. *Inorg. Chem. Front.* **2025**, *18*, 5315–5327.

[34] Wang, H.; Zhao, N.; Bi, Z. J.; Gao, S. H.; Dai, Q. S.; Yang, T. T.; Wang, J. W.; Jia, Z. Q.; Peng, Z. Q.; Huang, J. Y. et al. Clear representation of surface pathway reactions at Ag nanowire cathodes in all-solid Li-O_2 batteries. *ACS Appl. Mater. Interfaces* **2021**, *13*, 39157–39164.

[35] Zhang, P.; Han, B.; Yang, X. M.; Zou, Y. C.; Lu, X. Z.; Liu, X.; Zhu, Y. M.; Wu, D. J.; Shen, S. C.; Li, L. et al. Revealing the intrinsic atomic structure and chemistry of amorphous LiO_2-containing products in Li-O_2 batteries using cryogenic electron microscopy. *J. Am. Chem. Soc.* **2022**, *144*, 2129–2136.

[36] Liu, Y. J.; Ju, Z. J.; Zhang, B. L.; Wang, Y.; Nai, J. W.; Liu, T. F.; Tao, X. Y. Visualizing the sensitive lithium with atomic precision: Cryogenic electron microscopy for batteries. *Acc. Chem. Res.* **2021**, *54*, 2088–2099.

[37] Gao, Z. Y.; Yao, J. M.; Yan, J. T.; Sun, J.; Du, C. C.; Dai, Q. S.; Su, Y.; Zhao, J.; Chen, J. Z.; Li, X. M. et al. Atomic-scale cryo-TEM studies of the electrochemistry of redox mediator in Li-O_2 batteries. *Small* **2024**, *20*, 2311739.

[38] Suzuki, J.; Omae, O.; Sekine, K.; Takamura, T. Li mass transfer through a metallic Ag film covering on a carbon fiber anode. *Solid State Ionics* **2002**, *152–153*, 111–118.

[39] Suzuki, J.; Sekine, K.; Takamura, T. Evaluation of the diffusion coefficient of Li in Ag using a Li^+ sensor electrode mounted in a bipolar cell. *Electrochemistry* **2006**, *74*, 303–308.

[40] Dorai, A.; Kuwata, N.; Takekawa, R.; Kawamura, J.; Kataoka, K.; Akimoto, J. Diffusion coefficient of lithium ions in garnet-type $Li_{6.5}La_3Zr_{1.5}Ta_{0.5}O_{12}$ single crystal probed by ^7Li pulsed field gradient-NMR spectroscopy. *Solid State Ionics* **2018**, *327*, 18–26.

[41] Sun, X. Y.; Hou, Z. P.; He, P.; Zhou, H. S. Recent advances in rechargeable Li-CO_2 batteries. *Energy Fuels* **2021**, *35*, 9165–9186.

[42] Jin, S.; Ye, Y. D.; Niu, Y. J.; Xu, Y. S.; Jin, H. C.; Wang, J. X.; Sun, Z. W.; Cao, A. M.; Wu, X. J.; Luo, Y. et al. Solid-solution-based metal alloy phase for highly reversible lithium metal anode. *J. Am. Chem. Soc.* **2020**, *142*, 8818–8826.

[43] Kim, J.; Phiri, I.; Ryou, S. Y. Synergistically stabilizing thin Li metal through the formation of a stable and highly conductive solid electrolyte interface and silver-lithium alloy. *ACS Appl. Mater. Interfaces* **2023**, *15*, 46765–46774.

[44] Chen, Y. L.; Li, J. F.; Lu, B. Y.; Liu, Y. Q.; Mao, R.; Song, Y. Z.; Li, H. T.; Yu, X. Q.; Gao, Y. Z.; Peng, Q. et al. Activated Co in thiospinel boosting Li_2CO_3 decomposition in Li-CO_2 batteries. *Adv. Mater.* **2024**, *36*, 2406856.

[45] Chen, H. X.; Li, X. J.; Liu, Z. X.; Xu, Y. Y.; Yan, Y. G.; Li, P.; Chang, K.; Huang, X. L.; He, J. P.; Wang, T. Ferrocene-based nickel metal-organic framework nanosheets as efficient, long-cycle cathode catalyst for Li-CO_2 battery. *Adv. Funct. Mater.* **2025**, *35*, 2412387.

[46] Yang, T. T.; Jia, P.; Liu, Q. N.; Zhang, L. Q.; Du, C. C.; Chen, J. Z.; Ye, H. J.; Li, X. M.; Li, Y. S.; Shen, T. D. et al. Air-stable lithium spheres produced by electrochemical plating. *Angew. Chem., Int. Ed.* **2018**, *57*, 12750–12753.

[47] Stephan, O.; Ajayan, P. M.; Colliex, C.; Redlich, P.; Lambert, J. M.; Bernier, P.; Lefin, P. Doping graphitic and carbon nanotube structures with boron and nitrogen. *Science* **1994**, *266*, 1683–1685.

[48] Du, F. M.; Zhao, N.; Li, Y. Q.; Chen, C.; Liu, Z. W.; Guo, X. X. All solid state lithium batteries based on lamellar garnet-type ceramic electrolytes. *J. Power Sources* **2015**, *300*, 24–28.

[49] Kresse, G.; Furthmüller, J. Efficiency of *ab-initio* total energy calculations for metals and semiconductors using a plane-wave basis set. *Comput. Mater. Science* **1996**, *6*, 15–50.

[50] Kresse, G.; Furthmüller, J. Efficient iterative schemes for *ab initio* total-energy calculations using a plane-wave basis set. *Phys. Rev. B* **1996**, *54*, 11169–11186.

[51] Perdew, J. P.; Burke, K.; Ernzerhof, M. Generalized gradient approximation made simple. *Phys. Rev. Lett.* **1996**, *77*, 3865–3868.

[52] Blöchl, P. E. Projector augmented-wave method. *Phys. Rev. B* **1994**, *50*, 17953–17979.

[53] Kresse, G.; Joubert, D. From ultrasoft pseudopotentials to the projector augmented-wave method. *Phys. Rev. B* **1999**, *59*, 1758–1775.